IOP Publishing Plasma Sources Science and Technology

Plasma Sources Sci. Technol. **24** (2015) 065009 (14pp) doi:10.1088/0963-0252/24/6/065009

Properties of microplasmas excited by microwaves for VUV photon sources

James E Cooley[1,3], Randall Urdahl[1,4], Jun Xue[1,5], Mark Denning[1], Peng Tian[2] and Mark J Kushner[2]

[1] Agilent Laboratories, Agilent Technologies, Santa Clara, CA, 95051, USA
[2] University of Michigan, Dept. of Electrical and Computer Engineering, 1301 Beal Ave., Ann Arbor, MI 48109-2122, USA

E-mail: jimmycooley@gmail.com, randall_urdahl@sbcglobal.net, nkxuejun@hotmail.com, mark.denning@agilent.com, tianpeng@umich.edu and mjkush@umich.edu

Received 4 August 2015, revised 15 September 2015
Accepted for publication 30 September 2015
Published 27 October 2015

Abstract

Microplasma sources typically take advantage of pd (pressure × size) scaling by increasing pressure to operate at dimensions as small as tens of microns. In many applications, low pressure operation is desirable, which makes miniaturization difficult. In this paper, the characteristics of low pressure microplasma sources excited by microwave power are discussed based on results from experimental and computational studies. The intended application is production of VUV radiation for chemical analysis, and so emphasis in this study is on the production of resonant excited states of rare gases and radiation transport. The systems of interest operate at a few to 10 Torr in Ar and He/Ar mixtures with cavity dimensions of hundreds of microns to 1 mm. Power deposition is a few watts which produces fractional ionization of about 0.1%. We found that production of VUV radiation from argon microplasmas at 104.8 nm and 106.7 nm saturates as a function of power deposition due to a quasi-equilibrium that is established between the electron temperature (that is not terribly sensitive to power deposition) and the population of the Ar(4s) manifold.

Keywords: microplasma, VUV radiation, diagnostics, modeling

(Some figures may appear in colour only in the online journal)

I. Introduction

Microplasma sources, plasmas having sizes of <1 mm, typically leverage pd (pressure × dimension) scaling to achieve their small size [1–4]. By operating at higher pressures up to 1 atm, smaller dimensions are enabled. However, in many applications, microplasma-sized sources are required at lower pressures, a few Torr or less. Operating in this regime is problematic due to the high rate of diffusion loss which must then be balanced by a high specific power deposition. These plasma sources are also difficult to ignite and to sustain. An example of low pressure microplasmas is their use as an ionization source for chemical analysis. In this technology, the microplasma produces vacuum-ultraviolet (VUV) radiation which then selectively ionizes or dissociates the analyte at the entrance of a mass spectrometer or gas detector [5]. By using different gas mixtures (for example, different rare gases) in the microplasma discretely different VUV wavelengths can be produced. For example, a microplasma was used to produce VUV radiation as the fragmentation and ionization source for a high resolution time-of-flight mass spectrometer [6]. The microplasma was separately operated in Ar, Kr and Xe, producing VUV photons having energies of 11.6/11.8 eV, 10.0/10.6 eV and 8.4/9.6 eV. With this tunability of the energy of the ionization and fragmentation source by the choice of source gas, different sensitivities were produced in detecting various aromatic molecules.

The small size of the low-pressure microplasma devices, typically a few hundred microns, motivates the use of high excitation

[3] Present address: Mevion Medical Systems, 300 Foster St., Littleton, MA 01460, USA
[4] Present address: Nonlinear Ion Dynamics, LLC, 8 Harris Court, Suite A4, Monterey CA 93940 USA
[5] Present address: Applied Materials, 974E Arques Ave, Sunnyvale, CA 94085 USA

frequencies to limit the rate of loss of electrons and ions by drift in the electric field. In one configuration, a split-ring resonator operated at 2.45 GHz is used to create a large voltage across an electrode gap of a few hundred microns [7–9]. The use of arrays of split ring resonators to produce high pressure (up to atmospheric) microplasmas has been demonstrated by Hopwood *et al* [3, 10]. The low pressure device operates in a cavity having typical dimensions of a few hundred microns to 1 mm wide with a length of up to 1 cm. Two parallel electrodes terminating the split ring are aligned with the long dimension of the microcavity. Flow rates of rare gases and rare gas mixtures of 1–10 sccm produce pressures of several Torr inside the cavity. A small hole produces a gas plume containing ions and metastable atoms, and is also the aperture for the VUV emission. With a power of 4 W in a few Torr of argon, metastable Ar($1s_5$) densities exceeding 10^{12} cm^{-3} were measured in the plume [9]. VUV photon fluxes in excess of 10^{14} cm^{-2} s^{-1} were also measured.

In this paper, we report on results from a computational investigation of the plasma properties and VUV emission, and experimental measurements of excited state densities, in microwave excited microplasma devices sustained in argon and helium/argon mixtures. The configuration investigated is similar to that used for ionization sources for chemical analysis [7–9]. We found that the microplasma devices (MPDs) convert power deposited into the plasma into VUV emission with efficiencies of a few percent at low power deposition. In order to sustain the plasma at small values of pd, the excited state density must be large enough to take advantage of the efficiencies afforded by multi-step ionization. These conditions then lead to a near thermal equilibrium of the excited state densities with the electron temperature. The end result is a saturation in VUV emission with increasing power. The model and experimental techniques used in this investigation are discussed in sections II and III, followed by a discussion of plasma properties of the MPDs in section IV. Our concluding remarks are in section V.

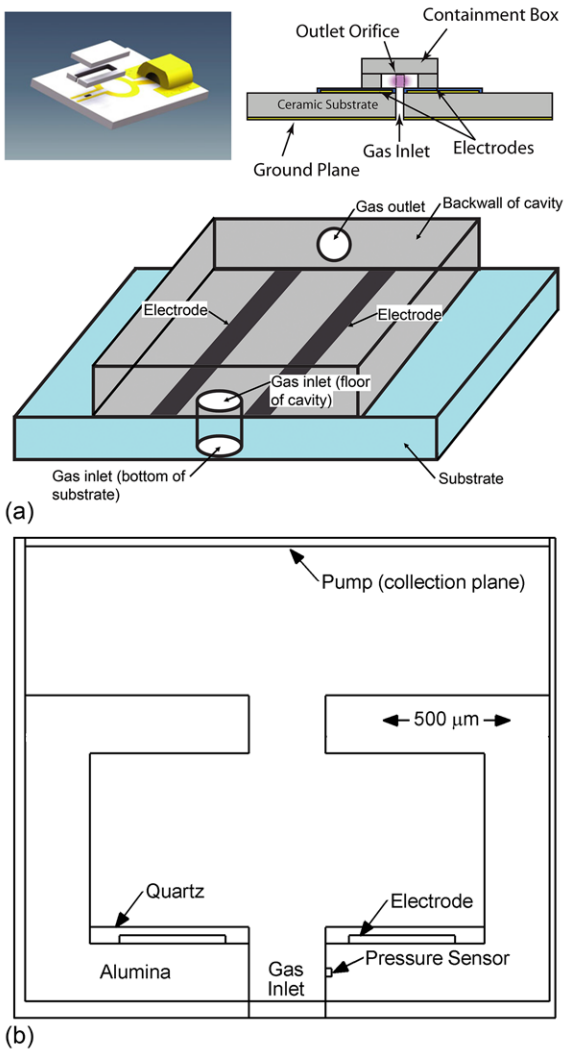

Figure 1. Schematics of the microwave excited, microplasma device. (a) Experimental configuration and (b) geometry used in the model.

II. Description of the model

The model used in this investigation is the Hybrid Plasma Equipment Model (HPEM), which is described in detail in [11]. The HPEM is a modular simulator which captures different physical phenomena into modules and exchanges information between those modules. In this study, the modules of the HPEM utilized are the Electron Energy Transport Module (EETM), Fluid Kinetics Module (FKM), Radiation Transport Module (RTM) and the Plasma Chemistry Monte Carlo Module (PCMCM).

The densities of all charged and neutral species, and the electric potential, are obtained from the FKM. Continuity, momentum and energy equations are integrated in time for all heavy particles (ions and neutrals). The electron density is obtained from integrating a continuity equation with fluxes provided by the Sharffeter-Gummel formulation which analytically provides the appropriate upwind fluxes depending on the sign of the local velocity. In this technique, by positive velocities contributions to the local change in density are provided by fluxes from the left of the cell. For negative velocities, contributions to the local change in density are provided by fluxes from the right of the cell. The pressure inside the cavity, measured at the location of the pressure sensor in figure 1, is held constant by adjusting the gas flow speed. The electric potential is obtained by solution of Poisson's equation using a semi-implicit technique assuming all potentials are electrostatic. Charge densities on surfaces are computed as being due to the fluxes of electrons and ions from the bulk plasma, secondary electrons leaving the surface and secondary electrons from other locations collected by those surfaces. All spatial derivatives are couched in finite-volume form. Acceleration techniques are used to speed the convergence of the simulation.

The electron Monte Carlo Simulation (eMCS) within the EETM is used to derive electron energy distributions (EEDs) for both bulk electrons and for the transport of sheath accelerated beam electrons. The algorithms used in the eMCS are discussed in detail in [12]. Briefly, electric fields from the FKM are recorded as a function of position and phase during the microwave cycle and cycle-averaged densities and source functions from the FKM are then used to advance trajectories of electron pseudoparticles in the eMCS. A particle-mesh

technique is used to resolve electron-electron collisions. Statistics are collected on the position and energy of electrons on each advance of their trajectories to produce EEDs, which are then combined with the electron densities from the FKM to produce electron impact sources as a function of position.

The eMCS is also used to compute separate electron impact source functions resulting from secondary electrons emitted from surfaces. The secondary electrons are produced by fluxes of ions, excited states and photons. The fluxes of ions and excited states are obtained from the FKM. The fluxes of photons are obtained from the RTM. Secondary electrons that fall in energy below ≈4 eV are removed from the eMCS and are used as source functions in the bulk electron continuity equation. Secondary electrons that are collected on surfaces are included as sources of negative charge.

Radiation transport in the RTM is addressed using Monte Carlo techniques [13, 14]. Photon pseudo-particles are isotropically launched from locations weighted by the density of the radiating states, for example, $Ar(1s_4)$ and $Ar(1s_2)$ in the case of argon plasmas. The photon pseudoparticles are advanced in line-of-site trajectories until the pseudoparticles hit a surface, are resonantly absorbed by ground state Ar or are non-resonantly absorbed through, for example, photoionization of excited states. The absorbed quanta of energy represented by the pseudoparticles are then either reradiated assuming partial frequency redistribution [14, 15] or are quenched. By quenching, we mean that the quanta of energy resident in the excited state undergoes a collision (e.g. electron impact ionization, super-elastic relaxation, Penning ionization) prior to that quanta of energy being reradiated as a photon. The lineshape function is a Voigt profile using the local gas temperature and collision frequency to determine broadening. The fluxes of photon-pseudoparticles are recorded as a function of position in the gas phase and on surfaces. The photon fluxes in the gas phase are used to produce photoionization sources which are then used in the FKM. The fluxes striking surfaces are used for sources of secondary electrons by photoelectron emission, and also represent the optical output of the device. A detailed description of the RTM appears in [16].

The simulation proceeds by integrating for 4 ns (or 10 microwave cycles) in the FKM, followed by a call to the RTM and the EETM. Within the EETM, electron trajectories are followed for 10 ns (or 25 microwave cycles). Since in this case we desire a periodic steady state, it is not necessary for the integration time to be the same in the different modules. This exchange between modules is performed for 200 iterations with acceleration being performed twice per iteration for the first 100 iterations for ions and for the first 190 iterations for neutrals.

The model for Ar consists of 10 species in addition to electrons: $Ar(3p^6)$ (ground state argon, also referred to as simply Ar), $Ar(1s_5)$, $Ar(1s_4)$, $Ar(1s_3)$, $Ar(1s_2)$, Ar(4p), Ar(4d), Ar^+, Ar_2^*, Ar_2^+. (In Racah notation, the first 4 excited states are, in order, $Ar(4s[3/2]_2)$, $Ar(4s[3/2]_1)$, $Ar(4s[1/2]_0)$, $Ar(4s[1/2]_1)$.) The Ar(4p) state is an effective lumped state representing Ar(4p,3d,5s,5p). The Ar(4d) state is an effective lumped state representing Ar(4d,6s,Rydberg) [17]. The reaction mechanism is the same as listed in [16]. The two resonance transitions $Ar(1s_4) \rightarrow Ar(3p^6)$ (106.7 nm) and $Ar(1s_2) \rightarrow Ar(3p^6)$ (104.8 nm), and the excimer radiation $Ar_2^* \rightarrow 2Ar$ (121 nm) are tracked in the RTM. The secondary electron emission coefficients from all surfaces are: 0.1 for ions, 0.03 for excited states and 0.01 for photons.

Mixtures of Ar/He were also investigated. The reaction mechanism for He/Ar mixtures has the following additional species: He, $He(2^3S)$, $He(2^1S)$, $He(2^3P)$, $He(2^1P)$, He(3s), He(3p) and He^+. He(3p) is a lumped state of all higher states. Emission from $He(2^1P) \rightarrow He$ (59.1 nm) is additionally considered in RTM. The reaction mechanism for He/Ar mixtures is the same as listed in [16].

III. Description of the experiment

Laser diode absorption spectroscopy was used to measure the column densities of $Ar(1s_3)$. The experimental technique is described in [9]. A laser diode from Sacher Lasertechnik emitting at 794.8 nm is directed through the MPD cavity through two holes and directed perpendicular to the electrodes. The laser has roughly a 1 nm tuning range around its center wavelength. The laser being used is mounted on a commercial laser head (TEC-052) and is driven by a laser current and temperature controller (Pilot PC 0500). The laser, having a linewidth of 0.01 pm, is tuned to measure the absorption of the $Ar(1s_3) \rightarrow Ar(2p_4)$ transition. A beam splitter diverts half of the laser intensity into a Fabry–Perot interferometer (free spectral range of 1.5 GHz, finesse <200, resolution <7.5 MHz), which is used to accurately calibrate the relative wavelength. The remainder of the beam is coupled to a single mode optical fiber. The output end of the fiber is mounted to a translation stage for alignment with the MPD. A lens, also mounted to the translation stage, focuses the beam to a 200 μm beam waist and this is the limit of the spatial resolution of this measurement.

Laser light was directed through holes in the MPD cavity made in the top roof and bottom substrate approximately at the mid-point along the axis. Measurements were made with the MPD mounted in a vacuum chamber. Laser light transmitted through the MPD cavity is detected with a Si photodetector. A neutral density filter is used to avoid pumping saturation effects. The signals of the interferometer and photo detector are acquired simultaneously and recorded by LabVIEW data acquisition software. More than 100 scans of each signal are accumulated and averaged to improve the signal to noise ratio. The absorption of the beam is measured and related to the absorption density by the Beer-Lampert law as described in [9]. The measurement provides a column density (atoms/cm^2) of the population difference between the $Ar(1s_3)$ and $Ar(2p_4)$ states. In interpreting the experimental data, we assumed that the density of the $Ar(1s_3)$ is much greater than that of the $Ar(2p_4)$.

IV. Microplasma characteristics

A schematic of the experimental device and the model geometry for the MPD are shown in figure 1. The microplasma

cavity is made of alumina ($\varepsilon/\varepsilon_0 = 9$) having a wall thickness of 230 μm. The inside dimensions of the cavity are 1.5 mm wide $\times$ 0.75 mm tall $\times$ 6 mm deep. The model, being 2D, does not resolve the full complexity of the MPD device. In the experimental device, the gas enters in through a channel between the bottom of the substrate to the bottom of the MPD cavity in the front of the device. The gas exits through a hole in the back wall of the MPD cavity. The electrodes are parallel to the long dimension, on the bottom of the MPD device. The model resolves the plane perpendicular to the long axis of the MPD in Cartesian coordinates without any axes of symmetry. The gas inlet in the model is at the bottom with a width of 230 μm and gas is exhausted out a nozzle on the top having the same width. The top boundary of the computational domain is the pump port and the plane upon which photon fluxes are collected to characterize the VUV output of the MPD. This surface will be referred to as the *top collection surface* in the remainder of the paper. The electrodes are 300 μm wide and are covered by quartz 30 μm thick. Since the actual thickness of the quartz is not resolved in the model, the dielectric constant of the overlying material is adjusted so that the capacitance of the dielectric covering the electrodes is the same as in the experiment. The outer boundary of the mesh is electrically grounded.

Since the inside surfaces of the microplasma cavity quickly charge and steady state conditions are being simulated, the proximity of the ground plane on the outside of the MPD does not affect the final plasma characteristics. This was verified by changing the capacitance (effective distance) between the microplasma cavity and the ground plane by changing the dielectric constant of the MPD walls. The depth of the MPD, 6 mm, only enters into the calculation in computing flow rates and power deposition where the total volume of the device is required, and in radiation transport where photons moving along the axis of the MPD striking the end walls are removed. An important distinction between the experimental MPD, as in [9], and the 2-d approximation here is the location of the gas inlet and nozzle. In the experimental MPD, the gas is injected through a hole in the bottom of the device. The hole for gas exit and VUV emission is in the end wall. In the model, the gas exits from the top along the entire axis of the MPD.

Voltage of equal amplitude is specified on the electrodes, 180 degrees out of phase. As such, the MPD appears to be a capacitive discharge in a push-pull configuration. The power deposition by each electrode is computed as a time average of the product of voltage and current, and the amplitude of the voltage is adjusted to deliver the desired power. These computations are done independently for each electrode assuming that half the power is deposited by each electrode. The base case operating conditions are a pressure of 4 Torr, power of 2 W and a nominal flow rate of 4 sccm. The flow rate is adjusted to provide the desired pressure as measured adjacent to the gas inlet port (as shown in figure 1). For computational convenience, the applied voltages are at a frequency of 2.5 GHz though in the experiment the frequency is 2.45 GHz. The voltage amplitude on each electrode to deliver 2 W in this base case is 17.9 V.

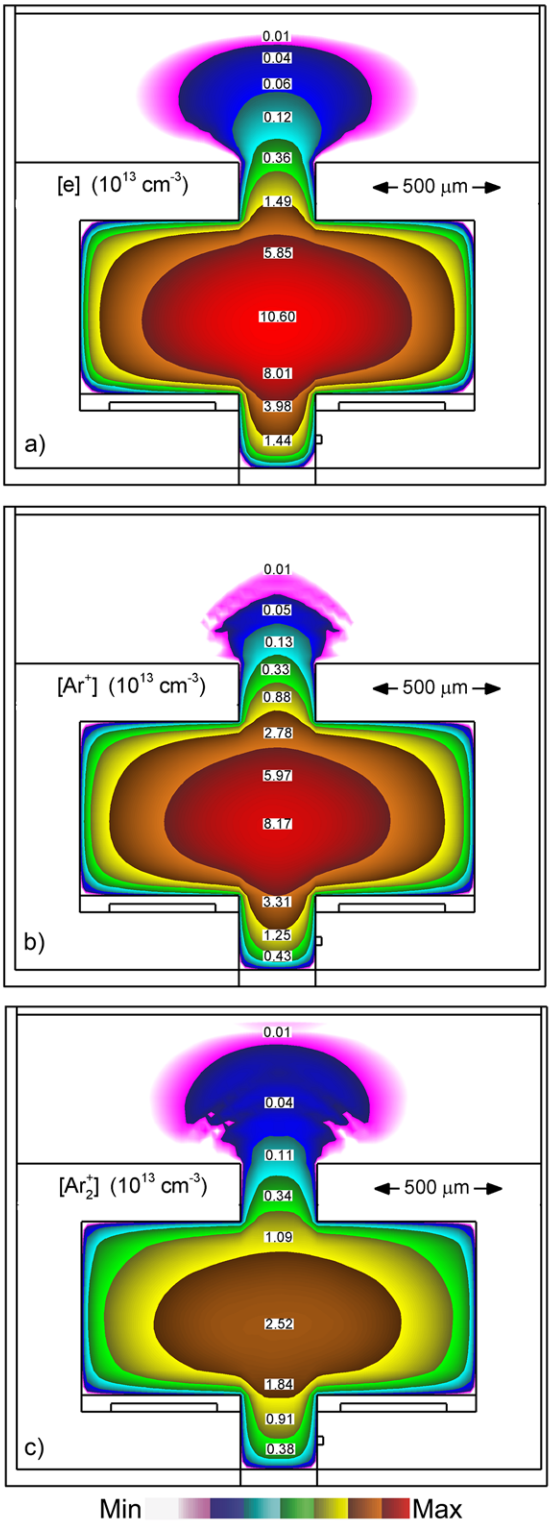

Figure 2. Plasma properties for the base case conditions (Ar, 4 Torr, 2 W, 4 sccm). (a) Electron density, (b) Ar^+ density and (c) Ar_2^+ density. The contour labels have the units indicated in each frame. A plume of plasma extends beyond the aperture.

IV.A. Plasma properties and optical emission in Ar microplasmas

The cycle averaged electron and ion densities are shown in figure 2. The electron temperature (T_e), ionization sources from

bulk electrons (S_e) and ionization sources from sheath accelerated secondary electrons from surfaces (S_{sec}) are shown in figure 3. The densities of the lowest metastable, Ar($1s_5$), lowest radiative state Ar($1s_4$) and highest excited state Ar(4d) are shown in figure 4. The peak electron density is 1×10^{14} cm^{-3} providing a peak partial ionization of about 0.2%. In spite of nonuniformities in the electron impact ionization source functions, the electrons have essentially a diffusion dominated profile inside the MPD cavity. The Ar_2^+ density constitutes 25% of the ion density in the center of the cavity. The dominant source of Ar_2^+ at this relatively low density is by associative Penning collisions of Ar(4d) with ground state Ar (maximum rate of 1.5×10^{20} cm^{-3} s^{-1}), which proceeds by virtue of the excitation energy of Ar(4d) being greater than the ionization potential of Ar_2^+ [18]. Other sources of Ar_2^+ include associative Penning reactions between two excited states (5.6×10^{18} cm^{-3} s^{-1}) and 3-body associative charge exchange (1.2×10^{17} cm^{-3} s^{-1}), whose rates are small in comparison to the associative Penning reaction of Ar(4d).

A plasma plume extends through the exit nozzle of the MPD cavity towards the observation plane, with ions being accelerated by the ambipolar electric fields produced by the peak plasma potential of 23 V in the center of the MPD. The axial electric field at the exit of the nozzle is 170 V/cm or an E/N (electric field/gas number density) of 210 Td (1 Td = 10^{-17} V cm^2). During the transition of ions from the MPD cavity to the collection plane, the dominant ion transitions from Ar^+ to Ar_2^+ due in large part to associative charge exchange. The drift speed of Ar^+ through the nozzle and to the collection plane is 1–2 $\times 10^5$ cm s^{-1} over a distance of about 1 mm at a time when the electric field is significantly decreasing. A shallow double-layer-like structure develops in the exit of the nozzle.

The electron temperature, T_e, is fairly uniform with values of 2.1–2.2 eV in the MPD cavity with a heating rate dominated by stochastic heating in front of each electrode. This uniform distribution of T_e is a consequence of the high electron thermal conductivity afforded by electron-electron collisions resulting from the high fractional ionization. T_e, decreases to 1.5 eV in the plume extending out the MPD cavity as the electron density decreases and thermal conductivity decreases. Recall that T_e is the average energy across the EED and so is dominated by low energy electrons that are typically below the excitation thresholds, at least from the ground state.

The bulk electron impact ionization rate, S_e, has a large contribution from multi-step ionization. The profile of S_e mirrors that of the lowest metastable state that has the highest density, Ar($1s_5$), as long as the electron temperature is above about 2 eV. The majority of the remainder of the bulk ionization is directly from the ground state. The peak value of ionization by bulk electrons is 1.5×10^{20} cm^{-3} s^{-1}. Although T_e does not significantly change from the cavity to the plume, the tail of the EED does decay in the plume (which is poorly reflected in the value of T_e). The behavior of the EED will be discussed below. The decay of the tail of the EED is reflected in the abrupt cut-off of S_e in the exit nozzle while T_e does not

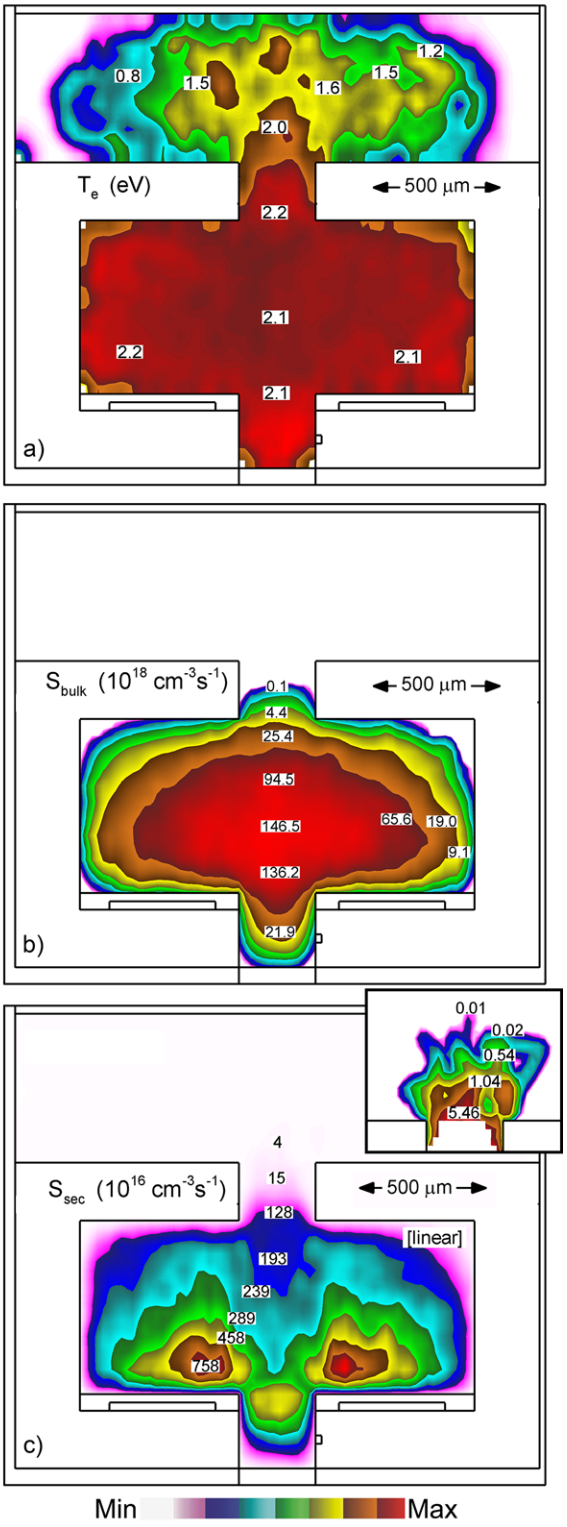

Figure 3. Plasma properties for the base case conditions (Ar, 4 Torr, 2 W, 4 sccm). (a) Electron temperature, (b) electron impact ionization source by bulk electrons and (c) electron impact ionization source by sheath-accelerated secondary electrons. The contour labels have the units indicated in each frame. The bulk ionization source terminates at the aperture due to the decay in the tail of the electron energy distribution. A few high energy secondary electrons scatter out of the aperture.

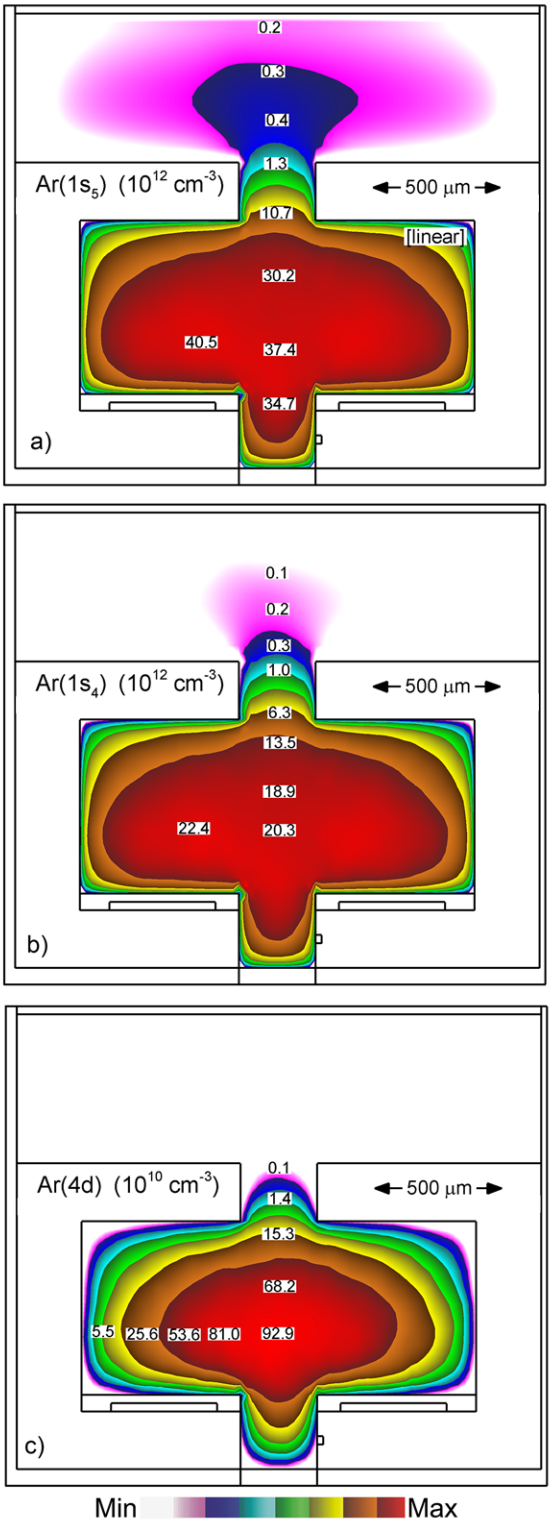

Figure 4. Excited state densities for the base case conditions (Ar, 4 Torr, 2 W, 4 sccm). (a) Ar($1s_5$), (b) Ar($1s_4$) and (c) Ar(4d), The contour labels have the units indicated in each frame. The metastable Ar($1s_5$) produces a plume beyond the microplasma cavity.

appreciably change. The ionization source due to sheath accelerated secondary electrons, S_{sec}, is maximum in front of each electrode, with peak values of 8×10^{18} cm^{-3} s^{-1}, or about 0.1 that of the bulk electrons. The trajectories of the secondary electrons are generally in the axial direction although there is some pendular motion of the electrons in the MPD cavity. However, due to the push-pull configuration of the electrodes, those sheath accelerated electrons which do reflect from the top interior surface of the MPD cavity also have a high likelihood of being collected by the other electrode. Due to some curvature of the sheath at the corner of the dielectric covering the electrodes and scattering in the gas, a flux of sheath accelerated electrons penetrates through the nozzle, providing a weak ionization source outside the MPD which is shown by the inset to figure 3(c).

The densities of Ar($1s_5$), Ar($1s_4$) and Ar(4d) are shown in figure 4. The peak density of Ar($1s_5$) is 4×10^{13} cm^{-3} in front of the electrodes where excitation by sheath accelerated secondary electrons is maximum and there is some lifting of the tail of the electron energy distribution, $f(\varepsilon)$, of the bulk electrons. The peak density of Ar($1s_4$) is 2×10^{13} cm^{-3}. The radiation trapping factor for Ar($1s_4$) in the middle of the cavity is 295 providing an effective lifetime of 2.5 μs. (The trapping factor for Ar($1s_2$) is 216, providing an effective lifetime of 0.42 μs.) Since the electron impact source functions for these states essentially mirrors that of the ionization, excitation largely occurs inside the MPD cavity. The short lifetime of the radiative state Ar($1s_4$), even when trapped, restricts its density to be largely inside the cavity where the excitation occurs. This is also the case for Ar(4d) which has a maximum density of 1×10^{12} cm^{-3}. The metastable state Ar($1s_5$) extends as a plume outside the cavity, carried in the advective gas flow that has a speed of 6.5×10^3 cm s^{-1} in the middle of the exit nozzle. Since Ar($1s_5$) and Ar($1s_4$) are rapidly collisionally mixed, a plume of Ar($1s_4$) also extends outside the cavity, whereas Ar(4d), which is not rapidly collisionally mixed with Ar($1s_5$), does not have a significant plume. There is some replenishment of the excited state manifold during the transit in the plume to the collection plane by dissociative recombination of Ar_2^+. This process accounts for about 50% of the excited state production at the top of the exit nozzle.

Infrared laser diode absorption measurements of Ar($1s_5$) densities in a similar MPD device were reported in [9]. The plume of the experimental MPD device emerges parallel and through the end wall at the end of the pair of electrodes. At the exit of the MPD, the Ar($1s_5$) and Ar($1s_3$) densities (metastable states) were measured as 1×10^{12} cm^{-3} and 3×10^{11} cm^{-3} [9]. The densities predicted by the model are 1.3×10^{12} cm^{-3} and 1.5×10^{11} cm^{-3}.

The average gas temperature in the center of the MPD is 550 K or about 225 K above ambient, and is 580 K adjacent to the electrodes. The majority of gas heating, 50–100 W cm^{-3}, results from symmetric charge exchange in the presheath above the electrodes. The large surface-to-volume ratio of the MPD moderates the temperature rise through heat conduction to the walls even though there is a temperature-jump boundary condition due to slip.

Cycle averaged $f(\varepsilon)$ are shown along the vertical axis of the MPD and horizontally 100 μm above the electrodes in figure 5. The $f(\varepsilon)$ as a function of height are 2-temperature distributions

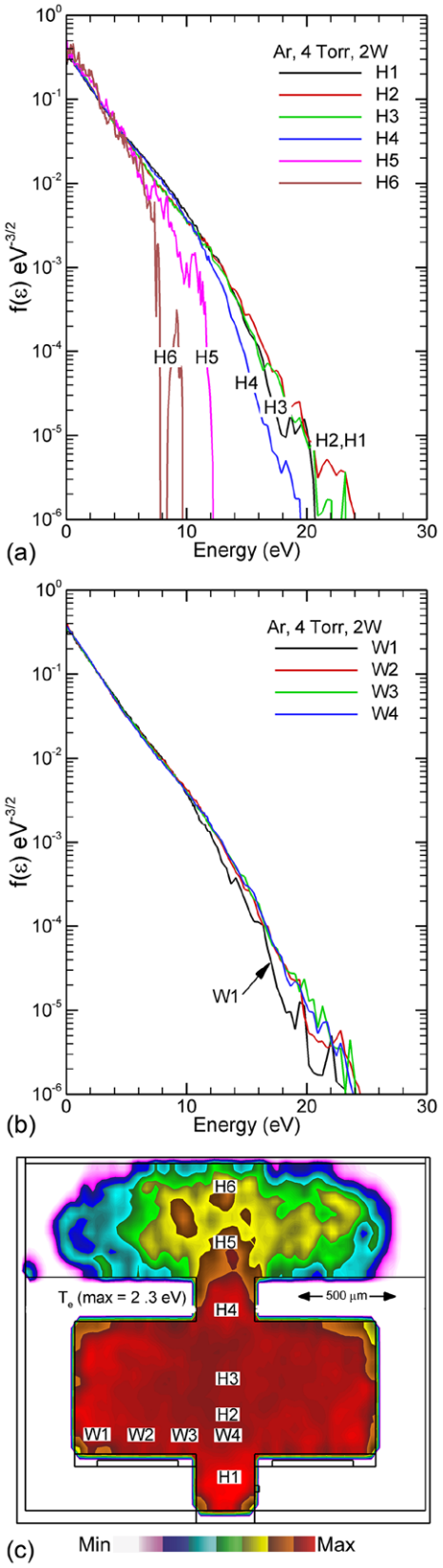

Figure 5. Electron energy distributions for the base case conditions (Ar, 4 Torr, 2 W, 4 sccm) at different locations in the cavity. (a) Along the vertical axis and (b) horizontally above the electrode. (c) The vertical locations where f(ε) are plotted are denoted by Hn and horizontal locations are denoted by Wn on a background of the electron temperature.

with the break-point being approximately at 12 eV, near the threshold energy of 11.6 eV for excitation of Ar($1s_5$). The high fractional ionization and the high rates of electron-electron collisions drives the $f(\varepsilon)$ towards a Maxwellian at lower energies and it is this part of $f(\varepsilon)$ that dominates the value of T_e. The electron density and thermal conductivity at the top of the nozzle and above the cavity are high enough to keep the bulk portion of the $f(\varepsilon)$ essentially Maxwellian. However, the rates of electron-electron collisions are insufficient to populate the tail of $f(\varepsilon)$. So at heights above the opening to the nozzle, the tail of the $f(\varepsilon)$ falls, which accounts for the rapid decrease in the electron impact ionization rate by bulk electrons. The $f(\varepsilon)$ as function of horizontal position above the electrodes are nearly indistinguishable in the bulk of the distribution, with the tail of $f(\varepsilon)$ moderately falling as the wall is approached.

The direction-averaged (or isotropic) VUV fluxes at 104.8 nm from Ar($1s_2$), 106.7 nm from Ar($1s_4$) and at 121 nm from Ar_2^* are shown in figure 6. (The rays that appear in these figures result from statistically heavy photon pseudoparticles in the simulation. These pseudoparticles represent an unusually large number of photons. These statistically heavy particles result from the photon pseudoparticles being uniformly distributed across the lineshape function [16].) The intracavity VUV flux at 104.8 nm is 3×10^{19} cm^{-2} s^{-1} or an intensity of 56 W cm^{-2}, which represents a considerable circulating optical intensity. At 106.7 nm, the flux is 1×10^{19} cm^{-2} s^{-1} (or an intensity of 19 W cm^{-2}). The mean free path at line center for reabsorption of the resonance radiation is about 0.1 μm which results in these lines being heavily trapped even for the small dimensions of the MPD cavity. The large circulating intensity within the cavity is dominantly radiation near line center which transports in a diffusional manner. That is, the quantum of energy represented by the photon is repeatedly emitted and reabsorbed with a mean-free-path about 1/1000 the size of the cavity. The radiation that strikes the wall or escapes through the top nozzle is composed of photons that are emitted in the wings of the lineshape where the mean free path is longer. Even these photons have some probability of reabsorption above the nozzle, which results in some diffusion-like transport. As a result, the resonant photon fluxes above the nozzle are not strictly line-of-sight out of the MPD cavity.

Although the VUV fluxes inside the MPD cavity are large, the photoionization cross sections from all excited states are not large, $\approx 10^{-19}$ cm^2 [19]. These small cross sections produces a rate of photoionization of 2–4 $\times 10^{14}$ cm^{-3} s^{-1} in the center of the MPD cavity. As a result, the contribution of photoionization of excited states by VUV radiation to the total rate of ionization is small. At low power deposition, 0.5 W, photoionization contributes only 10^{-5} of the total ionization. This contribution drops to 10^{-6} for a power deposition of 5 W, a consequence of the decrease in trapping factor at the higher power. Although the contribution of photoionization is small inside the cavity compared to electron impact ionization, in the periphery of the plume the rate of electron impact ionization falls to small values due to the fall in the tail of $f(\varepsilon)$, while there is still photoionization of the long lived metastable states by the VUV flux emanating from the MPD cavity. Although

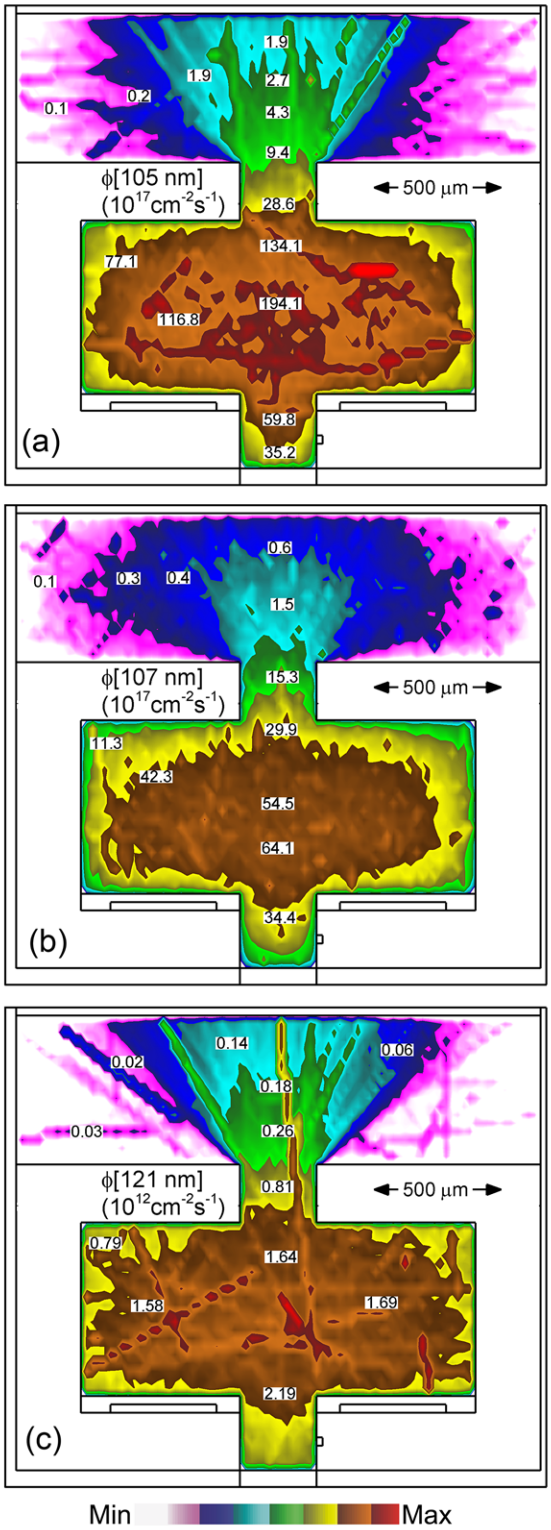

Figure 6. Direction averaged intensity of VUV radiation at (a) 104.8 nm, (b) 106.7 nm and (c) 121 nm.

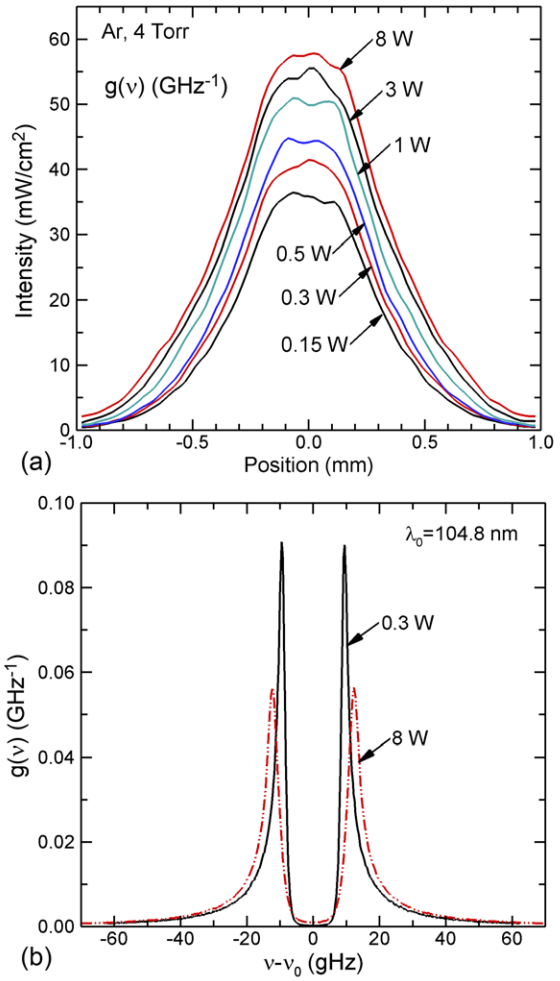

Figure 7. Radiative properties as a function of power deposition for Ar at 4 Torr. (a) Sum of the 104.8 nm and 106.7 nm VUV emission incident on the top collection surface. (b) Lineshape function for 0.3 and 8 W for 104.8 nm for radiation escaping the plasma.

the absolute magnitude of photoionization in the periphery of the plume is also small, 10^8–10^{10} cm^{-3} s^{-1}, photoionization may be comparable to or exceeding ionization by electron impact in the plume.

The peak random photon flux at 121 nm from Ar_2^* is considerably smaller than at the resonance lines, 8×10^{12} cm^{-2} s^{-1} or an intensity of 13 μW cm^{-2}. This flux is small (despite of the fact that the excimer radiation is not optically trapped) due to the much smaller peak density of Ar_2^*, 5×10^7 cm^{-3}, compared with the Ar(1s$_2$) and Ar(1s$_4$) radiative state densities. With the exception of a small amount of absorption from photoionization, the plasma is optically thin for the 121 nm radiation and so the transport of the excimer radiation is basically line-of-sight. There is no recirculation (or diffusional transport) of this radiation within the cavity and the radiation to the collection plane is line of sight from its radiating source.

The VUV intensity (sum of the 104.8 and 106.7 nm intensities) as a function of position on the top collection surface for different microwave powers, and optical line-shape functions for the 104.8 nm [Ar(1s$_2$) → Ar(3p^6)] transition are shown in figure 7. (The VUV flux is approximately 8×10^{14} cm^{-2} s^{-1} per mW cm^{-2}.) These data have been smoothed to lessen the statistical noise. The experimentally measured and predicted column densities of Ar(1s$_3$) are shown in figure 8. The column densities are the line integrated densities of excited states as measured by absorption spectroscopy. The peak optical powers (sum of the 104.8 and 106.7 nm fluxes) as a function of

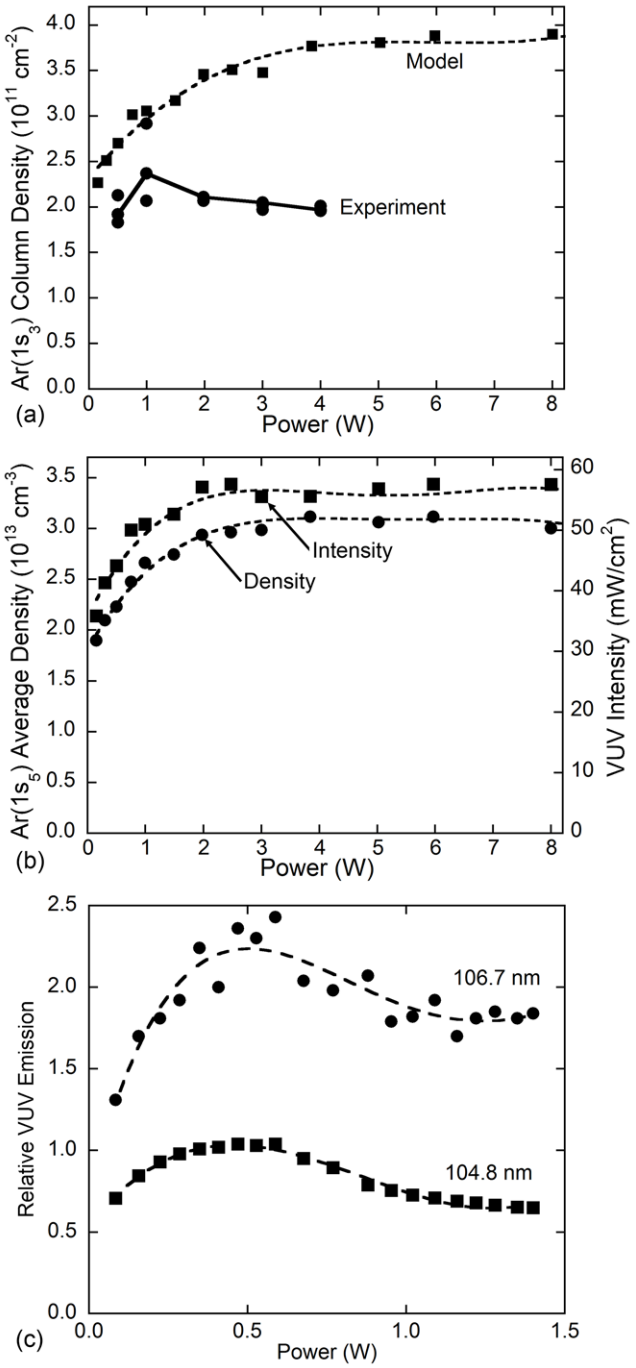

Figure 8. Densities of excited states and VUV emission in the Ar microplasma. a) Column density for $Ar(1s_3)$ as a function of power deposition measured by experiment and from the model. b) Model predictions of the $Ar(1s_5)$ density and the VUV output intensity as a function of power, and c) experimental relative VUV emission at 104.8 nm and 106.7 nm for similar conditions.

microwave power are also shown in figure 8. The peak VUV fluxes from the model onto the top collection surface in large part result from line of sight emission from the MPD cavity of photons in the wings of the lineshape function. (Line-of-sight from the center of the cavity corresponds to ±0.3 mm from the centerline.) Photons in the wings of the lineshape function have long mean free paths and so are optically thin. The fluxes that arrive at broader angles than line-of-sight from the interior of the MPD cavity result from absorption and re-emission of photons either in the nozzle or outside the cavity. The saturation of VUV emission with increasing power deposition can be severe and, in some cases, the VUV emission may decrease at higher power deposition. For example, relative values of experimentally measured VUV emission from Ar at 104.8 nm and 106.7 nm obtained with a photomultiplier tube are shown in figure 8(c). The conditions and device for the experimental are similar to that described above—2.8 Torr, 10 sccm.

The spectra, shown in figure 7(b), are heavily self-absorbed, an indication of radiation trapping that aligns with the computed radiation trapping factors of 180–400. For a power deposition of 2 W, the gas temperature in the middle of the MPD is 550 K which produces a Doppler width of $\Delta\nu_D$ =7.6 GHz, natural broadening of 80 MHz and pressure broadening of 8 MHz. The self-absorbed core of the lineshape function is well represented by the Doppler broadening. For a power deposition of 8 W, the trapping factors for the 106.7 nm [$Ar(1s_4) \rightarrow Ar(3p^6)$] transition having the longer natural lifetime, 8.4 ns, are about 150–160. The trapping factors for the 104.8 nm [$Ar(1s_2) \rightarrow Ar(3p^6)$] transition having the shorter natural lifetime, 2.0 ns, are 220–230. At a power deposition of 0.3 W, the trapping factors are 430–440 for the 106.7 nm transition and 200–210 for the 104.8 nm transition. The marked change in trapping factors is partly due to the change in gas temperature and ground state density. At 0.3 W, the mid-cavity gas temperature is 390 K and ground state absorber density is 9.6×10^{16} cm^{-3}, whereas at 8 W, the mid-cavity gas temperature is 890 K and ground state absorber density is 4.4×10^{16} cm^{-3}. The lower power deposition produces higher trapping factors due to there being a larger absorber density—the ground state. The higher temperature produces a wider Doppler width, $\Delta\nu_D$, that results in a broader self-absorbed core of the lineshape function and more VUV transmission in the wings of the lineshape relative to line center.

The spatially resolved VUV intensities (shown in figure 7) saturate with increasing power deposition above about 1 W. The maximum emitted VUV intensities and densities of $Ar(1s_3)$ as a function of MPD power deposition, shown in figure 8, also saturate with power deposition The experimentally measured column densities of $Ar(1s_3)$ have a small maximum at 1 W and saturate to 2×10^{11} cm^{-2} at higher powers. The predictions of the model show similar saturation with increasing power, with values about two times larger than in the experiment. Considering the 3D aspects of the experimental MPD that are not addressed in the model, the agreement is fairly good.

Over a range of power deposition of 0.15 to 8 W, the electron temperature is nearly constant—increasing from 1.9 eV at 0.15 W to 2.1 eV at 8 W. The peak electron density increases from 3×10^{13} cm^{-3} at 0.15 W to 2.1×10^{14} cm^{-3} at 8 W and the gas temperature increases from 370 K to nearly 900 K. The saturation in VUV output results, in part, from rarefaction of the gas. As the power increases and the gas temperature increases, the gas rarefies which reduces the density of the ground state and so decreases the maximum available density of radiators. The lower gas density also increases the rate of loss of charged particles by diffusion, which then reduces the rate of excitation of the resonant states by electron impact.

However the dominant factor in the saturation of the VUV output is a close coupling of the radiative states Ar($1s_2$) and Ar($1s_4$) with the metastable states Ar($1s_3$) and Ar($1s_5$). With the high plasma density, even at low power deposition and moderate radiation trapping, Ar($1s_5$) comes into near equilibrium with the ground state based on the electron temperature. The MPD cavity-averaged density of Ar($1s_5$) saturates at about 3×10^{13} cm^{-3} at a power of 2 W. (The local thermodynamic equilibrium (LTE) value of the Ar($1s_5$) density is about 1×10^{14} cm^{-3}.) With increasing power, and plasma density, superelastic and electron impact excitation collisions within the Ar(4s) manifold then drive Ar($1s_3$) and Ar($1s_4$) states into near equilibrium with Ar($1s_5$) which has the largest density. Ar($1s_3$) and Ar($1s_4$) are also progressively depleted by multistep ionization.

The voltage amplitudes on the electrodes increase from 9 V at 0.5 W to 37 V at 8 W. These low voltages are enabled by the large densities of excited states that improve efficiency of ionization through multistep ionization. No specific blocking capacitor was included in the circuit model and so the capacitance of the MPD electrode structure and walls serve as the blocking capacitor. Since the electrode configuration is, in principle symmetric, one would not expect large dc biases to develop and nor there to be large currents at the harmonics. The dc bias is negligible and within the noise of the Monte Carlo method. At 2 W, the dominant current is at the 1st harmonic with 1–2% of the current at the 2nd and 3rd harmonics, and 0.5–1% at the 4th and 5th harmonic. The dielectrics on top of the electrodes do charge negatively by up to −24 V at 8 W with respect to the underlying electrodes. This charging is due, in part, to bulk electrons accelerated from the opposite electrode that are collected in the push-pull configuration.

The oscillation of the plasma potential, dynamics of charging and discharging the wall capacitances, and the capacitance of the dielectric layer covering the electrodes result in energetic ion bombardment of the inside surfaces of the MPD cavity. For example, the ion energy distributions (IEDs) for Ar^+ and Ar_2^+ striking the dielectrics on top of the electrodes and averaged over the inside surface of the MPD are shown in figure 9 for 1 W and 8 W. Since the excitation frequency is far above the ion response time, the IEDs have only the single peak corresponding to the average sheath potential. The energies of the peaks in the IED for Ar^+ ions striking the inside dielectric surfaces of the MPD cavity are 14–15 eV. These energies correspond to the time averaged floating potential, slightly higher for the 8 W case to reflect the modestly higher T_e at the higher power. The energies of the peak for Ar_2^+ are 16–17 eV. The lower energies for Ar^+ are due to this ion undergoing symmetric charge exchange reactions in the sheath, whereas Ar_2^+ can only undergo elastic collisions. The maximum energies of both ions are 30 eV at 1 W and 40 eV at 8 W. The RC charging time of the sidewalls is sufficiently small, in large part due to the high conductivity of the plasma, that changes in the dielectric constant of the walls has little effect on the plasma and IEDs. The plasma characteristics are nearly independent of the dielectric constant of the walls over a range of $\varepsilon_r = 2$–20.

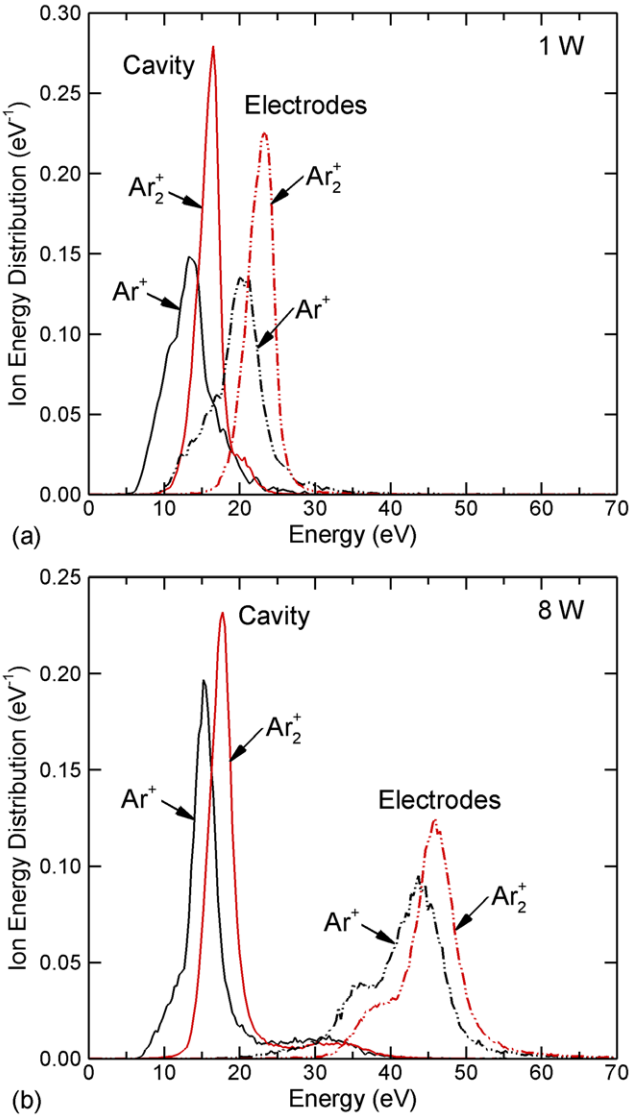

Figure 9. Ion energy distributions incident onto the walls of the microplasma cavity and to the surfaces above the electrodes for Ar discharges. (a) 1 W power deposition and (b) 8 W.

There are larger disparities in the IEDs striking the dielectrics over the electrodes between the low and high power cases. At 1 W, the energies of the peaks in the IED are 21 and 23 eV for Ar^+ and Ar_2^+, with maximum energies of 50 eV for an amplitude of applied voltage of 13 V. At 8 W, the energies of the peaks in the IED are 43 and 46 eV for Ar^+ and Ar_2^+, with maximum energies of 75 eV, for an amplitude of applied voltage of 27 V. Recall that the density of Ar_2^+ is about 20% of the total ions and the Ar_2^+ flux is about 15% of the total. So in spite of the higher energies of Ar_2^+ ions, the majority of the power delivered to surfaces by ions is from Ar^+.

The agreement between the experiment and the model has some uncertainty due to the model being 2D and there being 3D effects in the experiments. There are also uncertainties in the model due to uncertainties in the rate coefficients in the reaction mechanism. Although an exhaustive sensitivity study was not performed, we did perform a sensitivity study on selected reactions which are known to be important

or whose rates coefficients are known to be uncertain. The sensitivity was gauged by the density of Ar($1s_3$) at the center of the MPD cavity for 2 W power deposition. For example, when eliminating photoionization of all excited states, there was no significant change in the density of Ar($1s_3$)—less than 1%. A process that has significant effect on the ionization balance is associative ionization, $Ar(4d) + Ar \rightarrow Ar_2^+ + e$, with a rate coefficient 2.0×10^{-9} $(T_g/300)^{1/2}$ cm^3 s^{-1} (T_g is the gas temperature in K) [20]. When eliminating this reaction, the Ar($1s_3$) density increases by about 20%. This increase results from a reduction in the impedance of the plasma with the lower rate of ionization, which then requires a higher electron temperature to deliver the desired 2 W. The rate of formation of Ar($1s_3$) then increases with the increase in T_e. The rates of electron and heavy particle collisional mixing of the 4 levels in the Ar(4s) manifold are also somewhat uncertain. (See [16] for the sources of all such collision rates.) When increasing the heavy particle mixing rate coefficients by a factor of 2, the Ar($1s_3$) density does not significantly change. When increasing the electron impact cross sections for mixing by a factor of 2, the the Ar($1s_3$) density increases by 15%. This increase comes at the expense of Ar($1s_5$) whose density decreases with more rapid redistribution of density throughout the Ar(4s).manifold.

IV.B. He/Ar gas mixtures

It is a common practice in optimizing the performance of conventional lighting sources to use gas mixtures. For example, the common fluorescent lamp is typically an Ar/Hg mixture with the Ar fraction being 90–95%. The UV photons that excite the phosphor that produces the visible light are emitted by the Hg atoms. The purpose of the argon is to aid in the impedance matching to the power supply. The electron momentum collision frequency is dominated by the Ar which has the larger mole fraction. Inelastic electron collisions and power deposition are dominated by the Hg due to the lower threshold energies of its excited states and ion. There is similar motivation to use gas mixtures in microwave excited MPDs since their placement is at the end of a transmission line. Poor impedance matching would result in unwanted reflections on the transmission line. With this motivation, He/Ar gas mixtures were investigated.

The first-order effect of changing gas mixture in the MPD device, here operating at 4 Torr and 2 W, is changing the electron energy distribution, $f(\varepsilon)$. For example, $f(\varepsilon)$ at the center of the MPD are shown in figure 10(a) for He/Ar mixtures with the fraction of Ar from 5% to 99%. The corresponding electron temperatures and densities, and the density of Ar($1s_2$) are in figure 10(b). The spatial distributions of excited states and plasma density do not appreciably change when varying power with pure argon. These spatial distributions do change when changing mole fraction of Ar in He/Ar. The values shown in figure 10 are spatial averages inside the MPD cavity. With small fractions of Ar, the tail of $f(\varepsilon)$ is mildly cut-off at the inelastic threshold for excitation of He($^3S_1$) at 19.8 eV. As the mole fraction of Ar increases

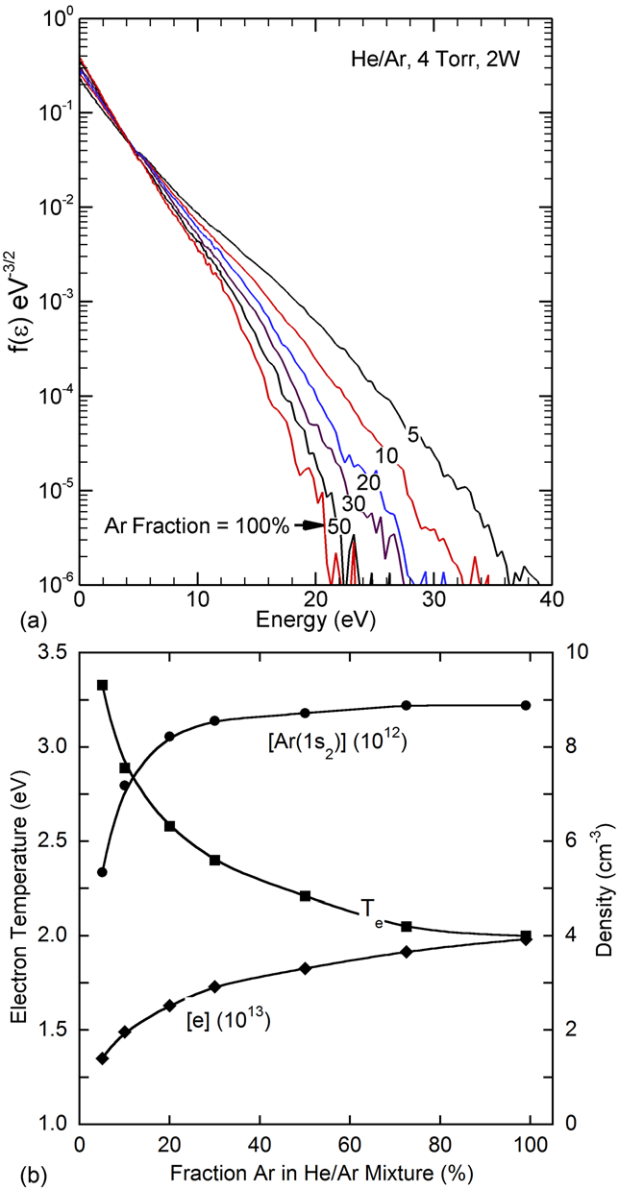

Figure 10. Plasma properties for microplasmas sustained in He/Ar mixtures (4 Torr, 2 W). (a) Electron energy distributions in the middle of the microplasma cavity for different Ar fractions. (b) Electron temperature, electron density and density of Ar($1s_2$) as a function of Ar fraction.

upwards from 5%, the energy of the cut-off switches to 11.6 eV, the inelastic threshold for excitation of Ar($1s_5$). This transition has largely occurred by a mole fraction of 30–50% argon. T_e decreases from 3.3 eV at an argon fraction of 5% to 2.2 eV at 50%. Higher mole fractions of Ar produce only a small decrease in T_e, to 2.0 eV at 99%. The average density of Ar($1s_2$) increases from 5×10^{12} cm^{-3} to 8.6×10^{12} cm^{-3} when increasing the Ar fraction from 5–50%, after which there is only a nominal increase. The electron density increases with increasing Ar fraction with less saturation than for the excited state densities.

These results suggest that in the He/Ar mixture, the majority of power deposition is dissipated in Ar by mole fractions of 35–40%. The saturation in the Ar($1s_2$) density and

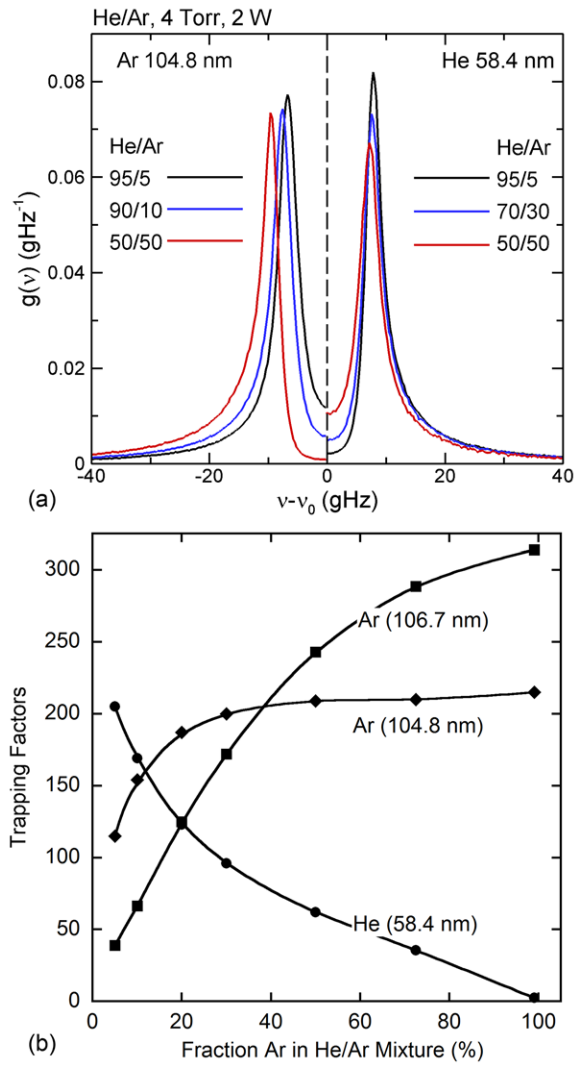

Figure 11. Optical properties for microplasmas sustained in He/Ar mixtures: (a) Lineshape functions for resonance radiation from Ar (104.8 nm) and He (58.4 nm) for different He/Ar mixtures. (b) Optical trapping factors for Ar (104.8 nm, 106.7 nm) and He (58.4 nm) as a function of Ar fraction.

lack of change in $f(\varepsilon)$ indicate that the losses by inelastic collisions with He are no longer important by this mole fraction. Any power dissipated in He by excitation or ionization is quickly transferred to Ar by Penning and charge exchange collisions. Experimental measurements of the column density of Ar($1s_3$) support this observation. In laser-diode-absorption experiments, the column density of Ar($1s_3$) increased in He/Ar mixtures by only 65% from an argon mole fraction of 10% to pure argon. The model predicts an increase of 40% over this range of mole fraction.

Changing the He/Ar gas mixture also affects radiation transport. For example, the spectra of the 104.8 nm emission from Ar and the 58.4 nm emission from He [He($^1P^0$) → He(^1S)], and their trapping factors predicted by the model are shown in figure 11. These lineshape functions are produced by the spectrally resolved photon pseudo-particles striking the top collection surface. Increasing the Ar mole fraction increases the optical depth for its resonant transition, thereby increasing the line center absorption which in turn increases trapping factors. This results in more observed emission coming from further in the wings of the lineshape function. The trend is the opposite for He as a decrease in its density reduces the self-absorption at line center and reduces its trapping factor. Some portion of the reduction in trapping factor results from quenching of the He($^1P^0$) upper level of the 58.4 nm emission by collisions with Ar. The natural radiative lifetime of He($^1P^0$) is 0.56 ns. The rate coefficient for Penning ionization of Ar by He($^1P^0$) at operating temperatures is 10^{-9} cm^3 s^{-1} [21, 22]. For an Ar fraction of 30% at 4 Torr, the lifetime of He($^1P^0$) for Penning reactions is about 40 ns, which is nearly the same as the effective lifetime of the 58.4 nm transition with a trapping factor of 100. So quenching reactions compete with radiative relaxation.

A desirable feature of MPDs for VUV sources is spectral purity. That is, the VUV spectrum is dominated by a single VUV emission line or closely spaced emission lines, as in the case of Ar (104.8, 106.7 nm). The use of gas mixtures introduces the possibility that the VUV spectrum will have emission from both sources. In the case of He/Ar mixtures, the VUV emission has contributions from the 58.4 nm transition in He, and the 104.8 and 106.7 nm transitions in Ar. The VUV intensities from Ar (sum of 104.8 and 106.8 nm transitions) and He incident onto the top collection surface are shown figure 12(a), and maximum values are shown in figure 12(b) as a function of Ar mole fraction in He/Ar mixtures. The intensities are shown in mW/cm^2. The VUV flux corresponding to 30 mW/cm^2 for emission from argon is 1.6×10^{16} cm^{-2} s^{-1}. The VUV flux for the same intensity of emission from He is 0.9×10^{16} cm^{-2} s^{-1}. For the He/Ar = 95/5 mixture, the VUV power flux from He is 25 mW cm^{-2}, about 80% that from Ar, 32 mW cm^{-2}. With increasing Ar mole fraction, the VUV emission from Ar increases to a maximum value of 55 mW cm^{-2} for an Ar mole fraction of 20%. At this mole fraction, the He emission has decreased to 1 mW cm^{-2}. The small decrease in the VUV power from Ar with mole fractions greater than 50% results from the decrease in electron temperature and increase in electron density for these mole fractions. The decrease in T_e reduces the rate coefficient for excitation of the resonant states while the increase in n_e increases the rate of mixing and quenching of the radiating states.

Spectral purity—a spectrum dominated by VUV emission from Ar—is obtained with moderate Ar mole fractions (20–30%). The dramatic decrease in the VUV emission from He has at least two components. The first is the increasingly cut-off electron energy distribution, $f(\varepsilon)$, with increasing Ar mole fraction, as shown in figure 10(a). From 5% to 30% Ar, the value of $f(\varepsilon)$ at 20 eV, the threshold for excitation of He, decreases by a factor of 100. Note that T_e decreases by only 0.7 eV over this range of Ar mole fraction due, in part, to the efficiency of electron-electron collisions at low energies which maintain a Maxwellian-like distribution. The second factor is the increasing rate of quenching of He excited states by the increasing Ar density which competes with radiative relaxation of the trapped resonance transition.

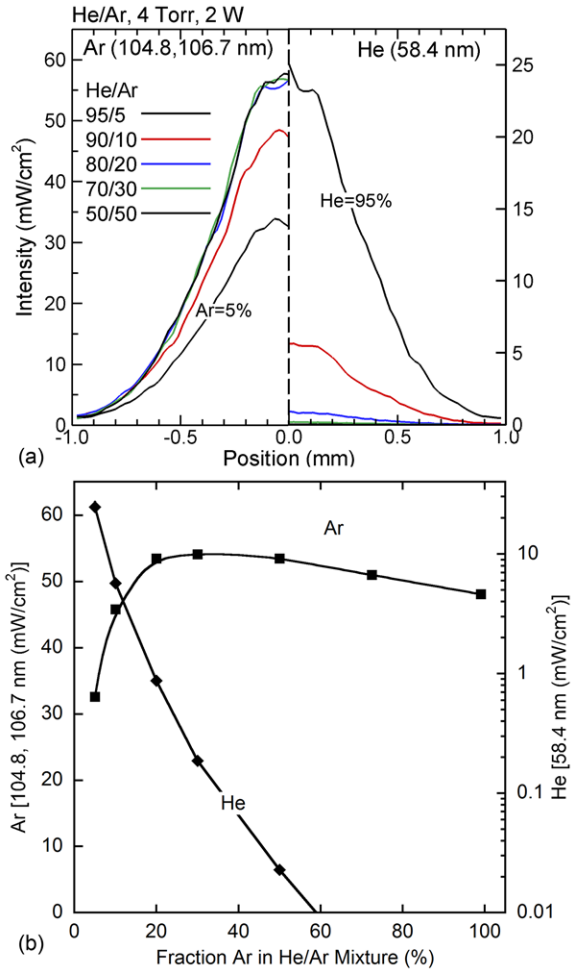

Figure 12. VUV intensities for microplasmas sustained in He/Ar mixtures. (a) Spatial profiles of VUV intensities incident on the top collection surface for different He/Ar mixtures, and (b) peak VUV intensities striking the top surface as a function of Ar fraction in He/Ar mixtures.

V. Concluding remarks

Microplasmas sustained by microwave power in rare gases and rare gas mixtures are convenient sources of VUV radiation for use in chemical analysis (e.g. ionization sources for mass spectrometers). The use of microplasmas for these applications typically requires the devices to operate at low pressure, a few Torr. Since the internal dimensions of the devices of interest are hundreds of μm to 1 mm, diffusion losses are large (pd $<$ 0.1–0.2 Torr-cm). Microwave excitation coupled with fully dielectric internal surfaces are able to sustain plasmas at few Torr with a few Watts of power deposition having plasma densities approaching 10^{14} cm^{-3} with electron temperatures of about 2 eV, values that are not particularly sensitive to power deposition. The resonant and metastable states of, for example, Ar come into a near equilibrium with the electron temperature, which results in the VUV emission saturating with power deposition above a few watts. The VUV fluxes are up to 40 mW cm^{-2} a few mm from the aperture of the microplasma cavity. VUV radiation is heavily trapped, producing self-absorbed lineshape functions, which in turn contribute to the radiative states coming into equilibrium. In mixtures of He/Ar, VUV emission from Ar optimized at 15–20% mole fraction of Ar, at which point the majority of power deposition was channeled into the argon and the electron temperature was elevated above the pure Ar discharge. Spectral purity for VUV emission from Ar is greater than 99%.

Acknowledgments

This work was supported by Agilent Technologies, Department of Energy Office of Fusion Energy Science (DE-SC0001319) and the National Science Foundation (CHE-1124724).

References

[1] Becker K H, Schoenbach K H and Eden J G 2006 Microplasmas and applications *J. Phys. D: Appl. Phys.* **39** R55
[2] Eden J G and Park S-J 2014 Microcavity and microchannel plasmas: general characteristics and emerging applications *Complex Plasmas* (*Springer Series on Atomic, Molecular, Optical and Plasma Physics* vol 82) (Switzerland 2014) ed M Bonitz *et al* p 373
[3] Hoskinson A R and Hopwood J 2014 Spatially resolved spectroscopy and electrical characterization of microplasmas and switchable microplasma arrays *Plasma Source Sci. Technol.* **23** 015024
[4] Becker K H, Kersten H, Hopwood J and Lopez J L 2010 Microplasmas: scientific challenges and technological opportunities *Eur. Phys. J.* D **60** 437
[5] Lopez-Avila V and Zoria M 2013 Identification of methylhexaneamine by GC high-resolution TOFMS and soft ionization *Forensic Sci. Intl* **231** 113
[6] Lopez-Avila V, Cooley J, Urdahl R and Theviswill M 2012 Determination of stimulants using gas chromatography/high-resolution time-of-flight mass spectrometry and a soft ionization source *Rapid. Commun. Mass Spectrom* **26** 2714
[7] Urdahl R, Cooley J E, Lee G S, Hidalgo A J and Guth M L 2014 *US Patent* 8,736,174 (May 27, 2014)
[8] Xue J, Urdahl R S and Cooley J E 2012 Plasma resonances in a microwave-driven microdischarge *Appl. Phys. Lett.* **100** 064102
[9] Xue J, Cooley J E and Urdahl R S 2012 Density of metastable atoms in the plume of a low-pressure argon microplasma *J. Phys.* D **45** 365201
[10] Wu C, Hoskinson A R and Hopwood J 2011 Stable linear plasma arrays at atmospheric pressure *Plasma Source Sci. Technol.* **20** 045022
[11] Kushner M J 2009 Hybrid modelling of low temperature plasmas for fundamental investigations and equipment design *J. Phys.* D **42** 194013
[12] Song S-H and Kushner M J 2012 Control of electron energy distributions and plasma characteristics of dual frequency, pulsed capacitively coupled plasmas sustained in Ar and Ar/CF_4/O_2 *Plasma Source Sci. Technol.* **21** 055028
[13] Herd M T, Lawler J E and Menningen K L 2005 Radiation trapping of the Hg 254 nm resonance line *J. Phys. D: Appl. Phys.* **38** 3304
[14] Lawler J E and Raizen M G 2013 Enhanced escape rate for Hg 254 nm resonance radiation in fluorescent lamps *J. Phys. D: Appl. Phys.* **46** 415204
[15] Parker G J, Hitchon W N G and Lawler J E 1993 Radiation trapping simulations using the propagator function method:

complete and partial frequency redistribution *J. Phys. B: At. Mol. Opt. Phys.* **26** 4643
[16] Tian P and Kushner M J 2015 Controlling VUV photon fluxes in low pressure inductively coupled plasmas *Plasma Source Sci. Technol.* **24** 035206
[17] Petrov M, Giuliani J L and Dasgupta A 2002 Electron energy deposition in an electron-beam pumped KrF amplifier: impact of beam power and energy *J. Appl. Phys.* **91** 2662
[18] Becker P M and Lampe F W 1965 Mass Spectroscopic study of the bimolecular formation of the diatomic argon ion *J. Chem. Phys.* **42** 3857
[19] McCann K J and Flannery M R 1977 Photoionization of metstable rate-gas atoms (He*, Ne*, Ar*, Kr*, Xe*) *Appl. Phys. Lett.* **31** 599
[20] Becker P M and Lampe F W 1965 *J. Chem. Phys.* **42** 2857
[21] Lindinger W, Schmeltekopf A L and Fehsenfeld F C 1974 Temperature dependence of de-excitation rate constants of He(2^3S) by Ne, Ar, Xe, H_2, N_2, O_2, NH_3, and CO_2 *J. Chem. Phys.* **61** 2890
[22] Schmeltekopf A L and Fehsenfeld F C 1970 De-excitation rate constants for helium metastable atoms with several atoms and molecules *J. Chem. Phys.* **53** 3173